

# 20

## Numerical benchmarks

**Theory:** Numerical benchmarks: testing of numerical codes for various problems. Examples of thermomechanical benchmarks. Manufactured solutions.

**Exercises:** Programming of models for various numerical benchmarks.

### 20.1 Code benchmarking: why should we spend time on it?

Benchmarking of a numerical code means comparing the numerical solution obtained from solving the system of linear equations with (i) analytical solutions, (ii) results of physical (analogue) experiments, (iii) numerical results from other (well established) codes and (iv) general physical considerations. Benchmarking of newly created numerical tools is sometimes very tedious, but is an absolutely necessary stage of code development as its purpose is to test the robustness of the code in a broad range of situations relevant to geodynamic modelling applications. For instance, if you plan to model shear heating processes in deforming rocks – make sure that your code provides the correct temperature changes related to mechanical energy dissipation; if you model subduction – make sure that your code handles correctly large viscosity contrasts and has no notable numerical diffusion of the temperature field and composition; if you intend to model self-gravitating planetary bodies – make sure that your code computes the correct gravity field etc. We should not be lazy and limit ourselves to one or two common benchmarks, such as the Rayleigh–Taylor instability and convection with constant viscosity, hoping that everything else will work automatically. No, it will not! Therefore, test your code on a broad range of challenging cases (several of which are discussed below), make it ‘screaming’ to explore its limitations and be creative in inventing and calibrating new numerical benchmarks. Then, in the end, you will be really proud of your ‘numerical child’. Many of the analytical solutions that can be used for testing of thermomechanical codes *for geodynamically relevant situations* can be taken from the textbook of Turcotte and Shubert (2002, 2014), which we will also use for constraining some of our numerical benchmarks.

Below we discuss details of several important benchmarks, which test various aspects of thermomechanical codes. These calibrating tests aim to verify the efficacy of numerical solutions for a variety of circumstances relevant to geodynamics. These include the following:

- (a) sharply discontinuous viscosity distribution (tests 1 and 2);
- (b) strain rate dependent viscosity (test 3);
- (c) non-steady-state development of temperature field (test 4);
- (d) shear heating for temperature-dependent viscosity (test 5);
- (e) advection of a sharp temperature front (test 6);
- (f) heat conduction for temperature-dependent thermal conductivity (test 7);
- (g) thermal convection with constant and variable viscosity (test 8);
- (h) elastic stress buildup and advection (tests 9 and 10);
- (i) localization of visco-elasto-plastic deformation (test 11);
- (j) kinetic to potential energy conversion during impact (test 12).

Of course this list is incomplete and many additional benchmarks exists, or can be invented. Yet, on performing the discussed benchmarks, we will at least get some confidence that we have created a state of the art numerical geodynamic modelling tool which correctly reproduces a number of challenging geodynamic models.

## 20.2 Test 1: Rayleigh–Taylor instability benchmark

This is a typical analytical solution based benchmark. To test the correctness of the numerical velocity solution for gravity driven flows, in the case of sharply heterogeneous density and viscosity fields, one can use a two-layer *Rayleigh–Taylor instability* model in a purely vertical gravity field (e.g. Ramberg, 1968) with a no-slip condition on the top and at the bottom and symmetry conditions along the vertical walls (Fig. 20.1a). An initial sinusoidal disturbance of the boundary between the upper ( $\eta_1, \rho_1$ ) and the lower ( $\eta_2, \rho_2$ ) layers of thicknesses  $h_1$  and  $h_2$ , respectively, has a small initial amplitude ( $\Delta A$ ) and a wavelength ( $\lambda$ ). Under this condition, the velocity of the diapiric growth ( $v_y$ ) is given by the relation (Ramberg, 1968)

$$\begin{aligned} \frac{v_y}{\Delta A} &= -K \frac{\rho_1 - \rho_2}{2\eta_2} h_2 g_y, \\ K &= \frac{-d_{12}}{c_{11} j_{22} - d_{12} i_{21}}, \\ c_{11} &= \frac{\eta_1 2\phi_1^2}{\eta_2 (\cosh 2\phi_1 - 1 - 2\phi_1^2)} - \frac{2\phi_2^2}{\cosh 2\phi_2 - 1 - 2\phi_2^2} \\ d_{12} &= \frac{\eta_1 (\sinh 2\phi_1 - 2\phi_1)}{\eta_2 (\cosh 2\phi_1 - 1 - 2\phi_1^2)} + \frac{\sinh 2\phi_2 - 2\phi_2}{\cosh 2\phi_2 - 1 - 2\phi_2^2}, \end{aligned} \quad (20.1)$$

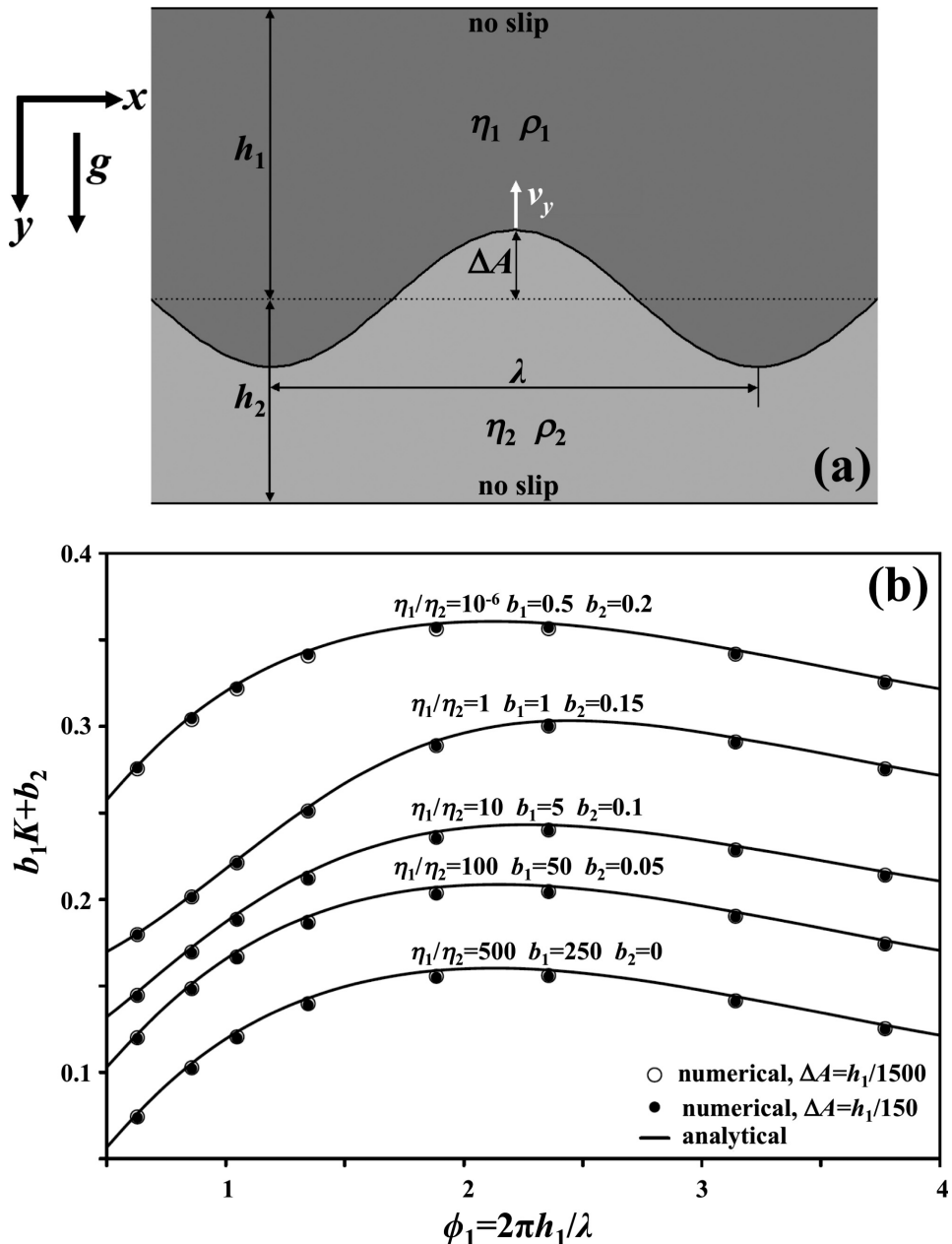


Fig. 20.1. Rayleigh–Taylor instability benchmark. (a) Initial setup. (b) Comparison of numerical (symbols) and analytical (lines, Eq. 16.1) solutions for the case of two layers with equal thicknesses ( $h_1 = h_2$ ). Arbitrary scaling coefficients  $b_1$  and  $b_2$  are used in (b) for plotting results computed at variable viscosity contrasts on the same diagram. The growth factor  $K$  for numerical cases is computed from the velocity field based on Eq. (20.1). Numerical results are calculated at resolutions of  $51 \times 51$  for nodes and  $250 \times 250$  for markers with the code **Variable\_viscosity\_Ramberg.m**.

$$i_{21} = \frac{\eta_1 \phi_2 (\sinh 2\phi_1 + 2\phi_1)}{\eta_2 (\cosh 2\phi_1 - 1 - 2\phi_1^2)} + \frac{\phi_2 (\sinh 2\phi_2 + 2\phi_2)}{\cosh 2\phi_2 - 1 - 2\phi_2^2},$$

$$j_{22} = \frac{\eta_1 2\phi_1^2 \phi_2}{\eta_2 (\cosh 2\phi_1 - 1 - 2\phi_1^2)} - \frac{2\phi_2^3}{\cosh 2\phi_2 - 1 - 2\phi_2^2},$$

$$\phi_1 = \frac{2\pi h_1}{\lambda},$$

$$\phi_2 = \frac{2\pi h_2}{\lambda},$$

where  $g_y$  is the vertical component of the gravitational acceleration,  $K$  is a dimensionless growth factor.

With a marker-in-cell method, a small layer boundary perturbation (much smaller than one grid step) can easily be prescribed on a subgrid scale by small sinusoidal (vertical) displacements of markers that are initially distributed regularly inside the numerical grid

$$\Delta A_m = \cos\left(2\pi \frac{x_m - 0.5L}{\lambda}\right) \Delta A, \quad (20.2)$$

where  $x_m$  and  $\Delta A_m$  are the horizontal coordinate and vertical displacement for a given marker  $m$ , and  $L$  is the horizontal width of the numerical model. For proper constraining of the numerical models, the relationship  $L = 2\lambda$  can be used together with free slip (i.e. horizontal symmetry) conditions on two vertical boundaries.

Figure 20.1b compares numerical and analytical solutions for the growth rate of the instability estimated for two layers of equal thickness (i.e.  $h_1=h_2$ ) at different values of  $\Delta A$ ,  $\lambda$  and  $\eta_1/\eta_2$ . Good accuracy at large variations of the disturbance wavelength and layer viscosity contrasts ( $\eta_1/\eta_2=10^{-6}$  to  $5\times 10^2$ ) suggests that the tested numerical code is capable of correctly modelling the velocity fields for gravity driven flows across a boundary with sharp changes in density and viscosity. Even very small subgrid perturbations of the horizontal boundary are properly captured by variations in relative position of markers via a bilinear density interpolation procedure from markers to nodes (Chapter 8). An example of the numerical setup for conducting the Rayleigh–Taylor instability benchmark is given by the code **Variable\_viscosity\_Ramberg.m**.

### 20.3 Test 2: falling block benchmark

This is a typical example of a benchmark which is based on general physical considerations. I personally like it very much, since it is simple to implement but creates challenging conditions to be handled numerically. In the case of an isolated rigid object, sinking in a low viscosity surrounding, the velocity of the object mainly depends on the viscosity of its surrounding (weakest medium). As was discussed in Chapter 18, this situation differs from

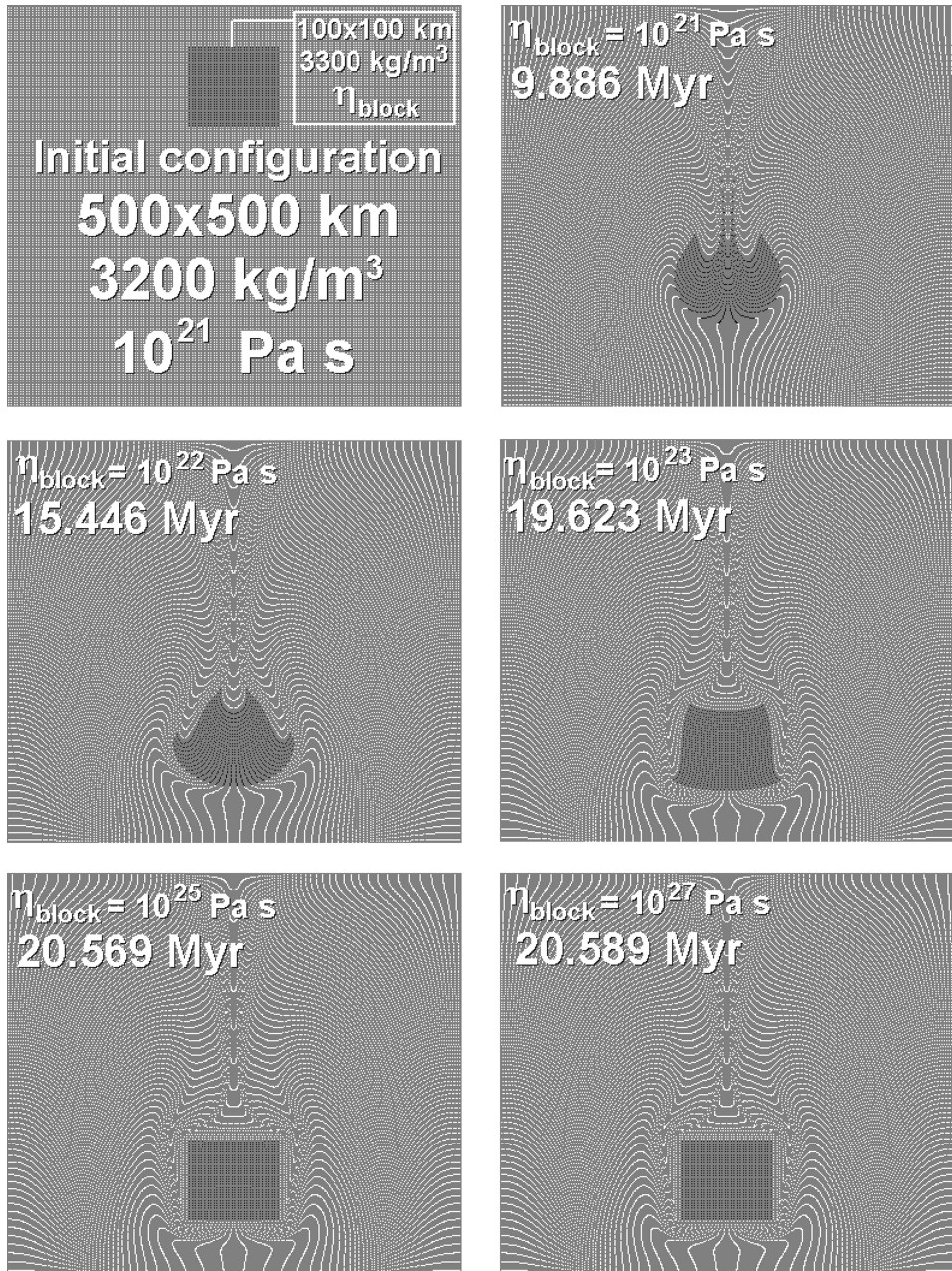


Fig. 20.2. Initial conditions (top left) and results of the numerical experiments for the falling block benchmark performed by Gerya and Yuen (2003a). Boundary conditions: free slip at all boundaries. Black and white dots represent positions of markers for the block and the medium, respectively. Grid resolution of the model is  $51 \times 51$  nodes, 22 500 markers.

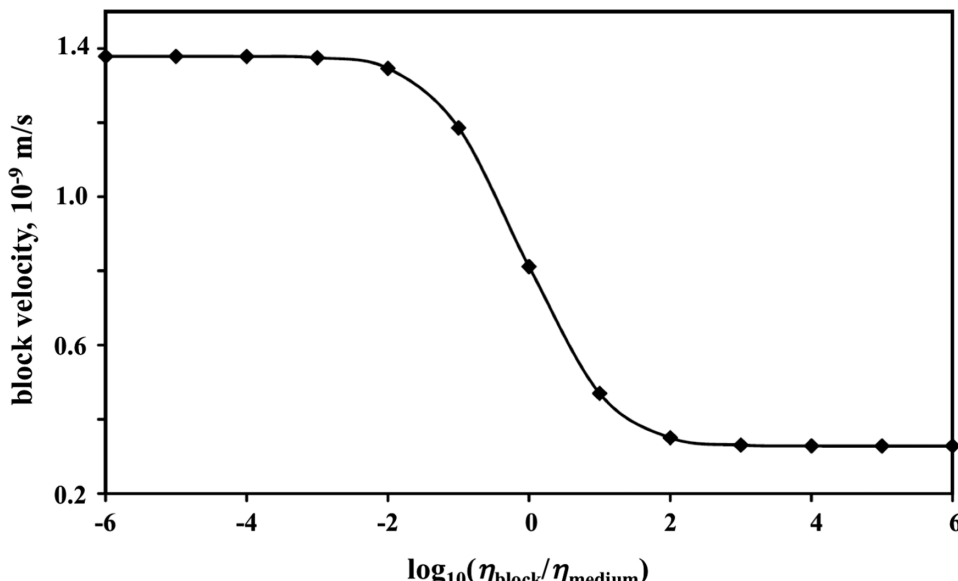


Fig. 20.3. Velocity of the rectangular block sinking in a viscous medium as a function of viscosity contrast between the block and the background medium. The model setup corresponds to Fig. 20.2 (top left). Numerical results are calculated at a resolution of  $51 \times 51$  nodes and  $250 \times 250$  markers with the code **Variable\_viscosity\_block.m**.

modelling the Rayleigh–Taylor instability where the strong layer is attached to the model boundaries and the velocity field is defined by the strongest medium. According to our physical intuition, (i) deformation of the block should vanish with increasing viscosity contrast (Fig. 20.2) and (ii) the sinking velocity at high viscosity contrasts should be independent of the absolute value of the viscosity of the block and should solely depend on that of the surrounding medium (Fig. 20.3). When using finite differences for solving the momentum equations, they should be formulated in a stress conservative manner (see Chapter 7). This test also proves the accurate conservation properties of a numerical procedure in terms of *preserving the block edges geometry* (Fig. 20.2) at large deformation and high ( $10^2$ – $10^6$ ) viscosity contrast between the stiffer block and the weak surroundings. An example of the numerical setup for conducting the falling block benchmark is given by the code **Variable\_viscosity\_block.m**.

#### 20.4 Test 3: channel flow with a non-Newtonian rheology

This test can be conducted to check the numerical solution of the momentum and continuity equations for flows with a strongly strain-rate/stress-dependent rheology, which is characteristic of dislocation creep (Ranalli, 1995). The computation is carried out for vertical flow of a non-Newtonian (with a power law index  $n$ ) viscous medium in a section of an

infinite vertical channel (Fig. 5.2) of width  $L$  in the absence of gravity. Boundary conditions are taken as follows: a given constant vertical pressure gradient  $\partial P / \partial y$  along the channel and no-slip conditions at the walls. The viscosity of the non-Newtonian flow is defined by the following rheological equation formulated in terms of second stress and strain rate invariants

$$2\dot{\varepsilon}_{II} = C_1(\sigma_{II})^n, \quad (20.3)$$

where  $C_1$  is a material constant in units of  $\text{Pa}^{-n} \cdot \text{s}^{-1}$ . Equation (20.3) can be reformulated in terms of effective viscosity (Chapter 6) as a function of second strain rate invariant

$$\eta_{eff} = \frac{\sigma_{II}}{2\dot{\varepsilon}_{II}} = C_1^{-1/n} (2\varepsilon_{II})^{1/n-1}. \quad (20.4)$$

Analytical solutions for the velocity and viscosity profiles across the channel are given by (Turcotte and Schubert, 2002; Gerya and Yuen, 2003a)

$$v_y = \frac{C_1}{n+1} \left( -\frac{\partial P}{\partial y} \right)^n \left[ \left( \frac{L}{2} \right)^{n+1} - \left( x - \frac{L}{2} \right)^{n+1} \right], \quad (20.5)$$

$$\eta_{eff} = \frac{\sigma_{II}}{2\dot{\varepsilon}_{II}} = \frac{\sigma'_{yx}}{2\dot{\varepsilon}_{yx}} = \frac{1}{C_1} \left( -\frac{\partial P}{\partial y} \right)^{1-n} \left( x - \frac{L}{2} \right)^{1-n}, \quad (20.6)$$

$$\frac{\partial P}{\partial y} = \frac{P_{end} - P_{beg}}{H}, \quad (20.7)$$

where  $P_{beg}$  and  $P_{end}$  are pressures at the beginning ( $x = 0$ ) and at the end ( $x = L$ ) of the channel section of height  $H$ , respectively. Figure 20.4 compares analytical and numerical (2D) solutions based on conservative finite differences with marker-in-cell techniques obtained with the code **Variable\_viscosity\_channel.m**. Numerical and analytical solutions overlap, implying high accuracy of the numerical method for modelling flows with strong lateral variations in viscosity caused by the non-Newtonian rheology. *Open channel boundary conditions* at the top and at the bottom imply an infinite vertical channel with constant vertical pressure gradients. These boundary conditions are programmed by defining  $P_{beg}$  and  $P_{end}$  in the first and the last row of pressure nodes, respectively, and prescribing  $\partial v_x / \partial y = 0$ ,  $\partial v_y / \partial y = 0$ , at the upper and lower boundaries of the model. Note that the vertical length of the channel section  $H$  used in Eq. (20.7) for computing the pressure gradient corresponds to the distance between the first and the last row of pressure nodes and not to the vertical length of the 2D model.

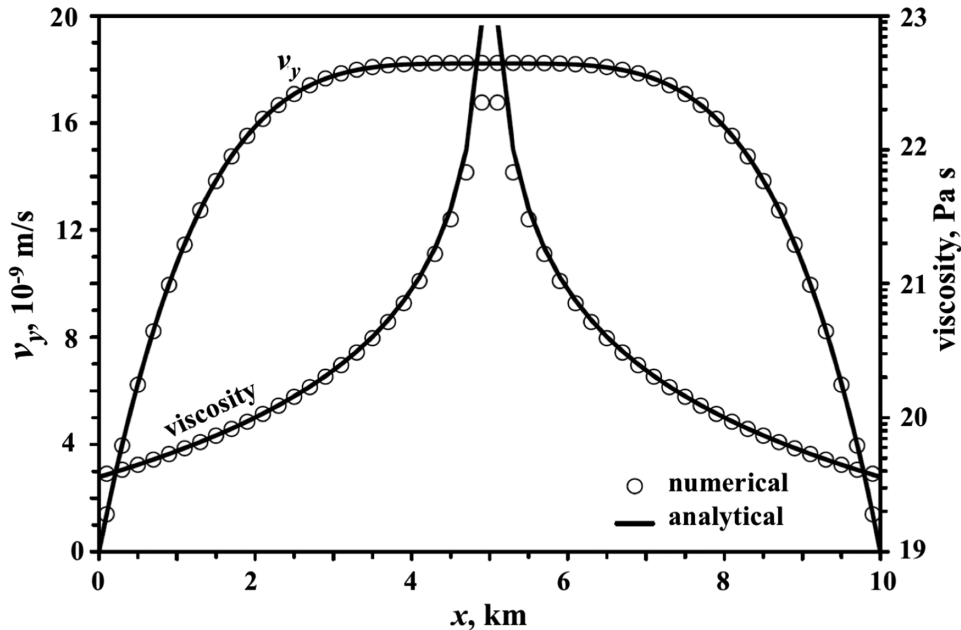


Fig. 20.4. Comparison of analytical and numerical solutions for the velocity and viscosity profiles across a channel with non-Newtonian flow rheology given by Eq. (20.3). Numerical results are calculated at the resolution of  $51 \times 21$  nodes and  $250 \times 100$  markers with the code **Variable\_viscosity\_channel.m** associated with this chapter. Model parameters:  $L = 10$  km,  $H = 9.5$  km,  $n = 3$ ,  $C_1 = 10^{-37} \text{ Pa}^{-3} \cdot \text{s}^{-1}$ ,  $P_{\text{beg}} = 10^9 \text{ Pa}$ ,  $P_{\text{end}} = 0$ .

## 20.5 Test 4: non-steady-state temperature distribution in a Newtonian channel

Here we describe another channel flow based benchmark. This one can be performed to test the numerical accuracy of solution of the time-dependent (non-steady-state) temperature equations in cases when heat advection is coupled with heat diffusion. The model corresponds to the vertical flow of a heat-conductive medium of constant viscosity  $\eta$  in a channel, in the absence of gravity. Boundary conditions are: a given constant vertical pressure gradient,  $\partial P / \partial y$  along the channel, non-slip conditions and  $T = \text{const} = T_o(y)$  and  $\partial T / \partial y = \text{const} = \partial T_o(y) / \partial y$  at the walls (Exercise 9.2). The initial conditions for the temperature distribution inside the model are  $T = T_o(y)$ ,  $\partial T / \partial y = \partial T_o(y) / \partial y$  and  $\partial T / \partial x = 0$ . The horizontal steady-state profile for vertical velocities,  $v_y$ , is defined by the equation which can be derived either from Eq. (20.5) with  $n = 1$  and  $C_1 = 1/\eta$  or from Eq. (5.30) with  $g_y = 0$

$$v_y = -\frac{1}{2\eta} \left( \frac{\partial P}{\partial y} \right) (Lx - x^2). \quad (20.8)$$

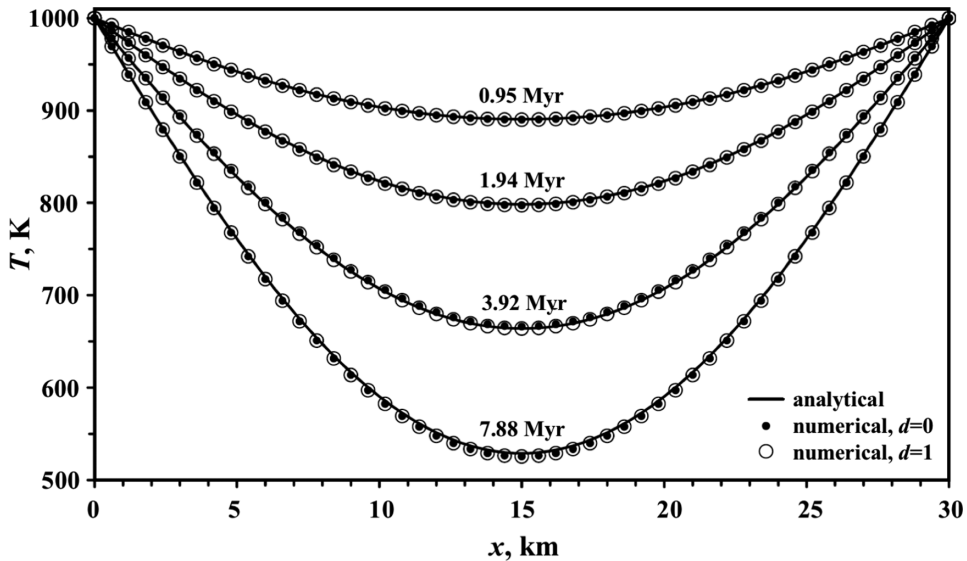


Fig. 20.5. Comparison of the analytical and numerical solutions for temperature profiles across the channel with constant viscosity. Numerical results are calculated at the resolution of  $51 \times 11$  nodes and  $250 \times 50$  markers with the code **Constant\_viscosity\_channel\_T.m**. Model parameters:  $L = 30$  km,  $H = 11.25$  km,  $\eta = 10^{19}$  Pa s,  $P_{\text{beg}} = 10^5$  Pa,  $P_{\text{end}} = 0$ ,  $\partial T / \partial y = 40$  K/km,  $T(y = 0) = 1000$  K.

The corresponding temperature changes in the channel with time are then given by the following series expansion (Gerya and Yuen, 2003a, it is typically enough to compute the first 10 terms of the expansion for an accurate solution)

$$\Delta T(x, t) = \sum_{m=1}^{\infty} F_m E_{mt} \sin \left[ \pi(2m - 1) \frac{x}{L} \right], \quad (20.9)$$

$$F_m = -8\xi \frac{L^2}{[\pi(2m - 1)]^3},$$

$$E_{mt} = L^2 \frac{1 - \exp \left\{ -\frac{\kappa t}{L^2} [\pi(2m - 1)]^2 \right\}}{\kappa [\pi(2m - 1)]^2},$$

$$\kappa = \frac{k}{\rho C_P},$$

$$\xi = -\frac{1}{2\eta} \left( \frac{\partial P}{\partial y} \right) \left( \frac{\partial T_o(y)}{\partial y} \right),$$

where  $\Delta T(x, t)$  is the temperature change as a function of the horizontal coordinate  $x$  and time  $t$ ;  $\kappa$  is a constant thermal diffusivity in units of  $\text{m}^2 \text{s}^{-1}$ . Equation (20.9) does not

account for shear heating: in this numerical test it is considered negligible. Figure 20.5 compares the analytical solution from Eq. (20.9) with the numerical solution obtained with the 2D thermomechanical code **Constant\_viscosity\_channel\_T.m**. Mechanical boundary conditions for the infinite vertical channel are the same as for the previous benchmark. A constant temperature gradient is used as a boundary condition for temperature nodes located at the upper and lower thermal boundaries, implying infinity of the thermal profile in the vertical direction. Figure 20.5 shows that numerical and analytical results coincide well for calculations performed both with ( $d = 1$ ) and without ( $d = 0$ ) numerical subgrid diffusion (Eqs. 10.15–10.19), implying robustness of the coupled thermomechanical solution for the case of non-steady-state heat conduction associated with heat advection.

## 20.6 Test 5: Couette flow with shear heating

This benchmark is designed to verify the numerical solution of the coupled momentum and temperature equations for flows with temperature-dependent rheology in the situation of strong shear heating (viscous dissipation). The analytical model setup corresponds to a vertical *Couette flow* (simple shear deformation in a laterally limited planar zone of width  $L$ ) in the absence of gravity. Boundary conditions are taken as follows: zero vertical pressure gradient,  $\partial P/\partial y = 0$  along the flow,  $v_y = 0$ ,  $T = T_0$  and  $\sigma_{yx} = \text{const} = \sigma_{xy}$ ,  $\partial T/\partial x = 0$  at the left and right walls, respectively. Viscosity of the flow is given by the following rheological equation (Turcotte and Schubert, 2002)

$$\eta = A \exp \left[ \frac{E_a}{RT_0} \left( 1 - \frac{T - T_0}{T_0} \right) \right],$$

where  $E_a$  is the activation energy,  $R$  is the gas constant and  $A$  is a pre-exponential rheological constant, which depends on the material. The analytical solution for steady temperature distribution  $T(x)$  inside the flow is given by the relation (Turcotte and Schubert, 2002)

$$x = \frac{L}{B} \ln \left[ \frac{(D + B)(C - B)}{(D - B)(C + B)} \right], \quad (20.10)$$

$$B = \ln \left[ \frac{1 + \left( 1 - \frac{2Br}{B^2} \right)^2}{1 - \left( 1 - \frac{2Br}{B^2} \right)^2} \right], \quad (20.11)$$

$$C = \left\{ 2[\phi_1 - \phi(x)]Br \right\}^{1/2}, \quad (20.12)$$

$$D = [2(\phi_1 - 1)Br]^{1/2}, \quad (20.13)$$

$$\phi(x) = \exp[\theta(x)], \quad (20.14)$$

$$\theta(x) = \frac{E_a[T(x) - T_0]}{RT_0^2}, \quad (20.15)$$

$$\phi_1 = \frac{B^2}{2Br}, \quad (20.16)$$

$$\phi_1 = \exp(\theta_1), \quad (20.17)$$

$$\theta_1 = \frac{E_a(T_1 - T_0)}{RT_0^2}, \quad (20.18)$$

$$Br = \frac{\left(\sigma'_{yx1}L\right)^2 E_a}{kART_0^2} \exp\left(-\frac{E_a}{RT_0}\right), \quad (20.19)$$

where  $Br$  is the non-dimensional Brinkman number,  $\theta$  is the non-dimensional temperature change,  $\sigma'_{yx1}$  is the shear stress that remains constant within the flow,  $k$  is the thermal conductivity of the flow medium,  $T_1$  is the temperature at the right wall of the flow (i.e. maximal temperature). Solving the non-linear equations (20.10)–(20.19) analytically for given values of  $k, L, A, E_a, T_0$  and  $\sigma'_{yx1}$  is non-trivial and the solution for  $T_1$  is not unique at a given value of  $\sigma'_{yx1}$ . Rather than defining  $\sigma'_{yx1}$ , non-negative values of  $B$  can be chosen and then the Brinkman number and shear stress in the channel can be computed from Eq. (20.11) and Eq. (20.19), respectively, as

$$Br = \frac{B^2}{2} \left[ 1 - \left( \frac{\exp B - 1}{\exp B + 1} \right)^2 \right], \quad (20.20)$$

$$\sigma'_{yx1} = \left[ Br \frac{kART_0^2}{L^2 E_a} \exp\left(\frac{E_a}{RT_0}\right) \right]^{1/2}. \quad (20.21)$$

Other unknown parameters can be computed from  $B$  and  $Br$  by using Eqs. (20.10)–(20.18). Based on such calculations, the dependence of the maximal non-dimensional temperature change in the channel  $\theta_1$  on the Brinkman number  $Br$  can be computed (Fig. 20.6a).

To test the Couette flow solution numerically, the constant vertical velocity boundary condition  $v_y = v_{y1}$  should be applied at the right boundary instead of  $\sigma'_{yx} = \sigma'_{yx1}$  used in the analytical model. The upper and lower boundary conditions are the same as in tests 3 and 4 but with zero vertical pressure and temperature gradients ( $P_{beg} = P_{end} = 0$  and  $\partial T / \partial y = 0$ ). This modification will ensure uniqueness of the numerical thermomechanical solution that becomes steady state in a finite number of time steps. The value of the parameter  $B$  should be computed iteratively with Eqs. (20.16)–(20.18) and (20.20) from the steady-state temperature ( $T_1$ ) at the right boundary (see the computing procedure in the end of the

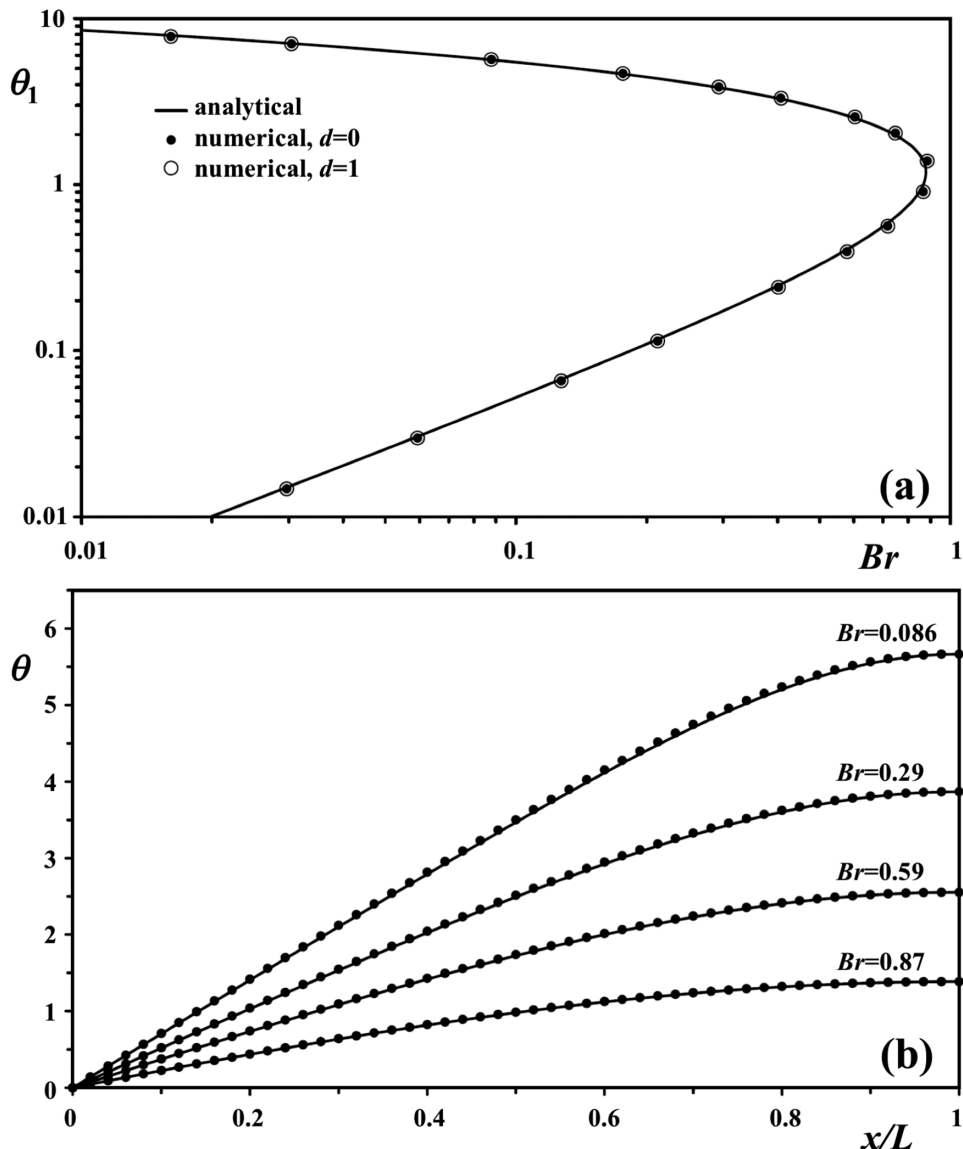


Fig. 20.6. Comparison of analytical and numerical results for a case of steady-state Couette flow with temperature-dependent viscosity (see Eq. 20.9) and shear heating. (a) Maximal temperature change within the flow  $\theta_1$  (Eq. 20.18) versus Brinkman number  $Br$  (Eq. 20.19). (b) Distribution of temperature changes  $\theta$  (Eq. 20.15) across the flow at different values of Brinkman number. Numerical results are calculated at a resolution of  $51 \times 11$  nodes and  $250 \times 50$  markers with the code **Variable\_viscosity\_Couette\_T.m** associated with this chapter. Model parameters:  $L = 30$  km,  $H = 11.25$  km,  $A = 10^{15}$  Pa s,  $E_a = 150$  kJ/mol,  $k = 2$  W/(m K),  $T_0 = 1000$  K.

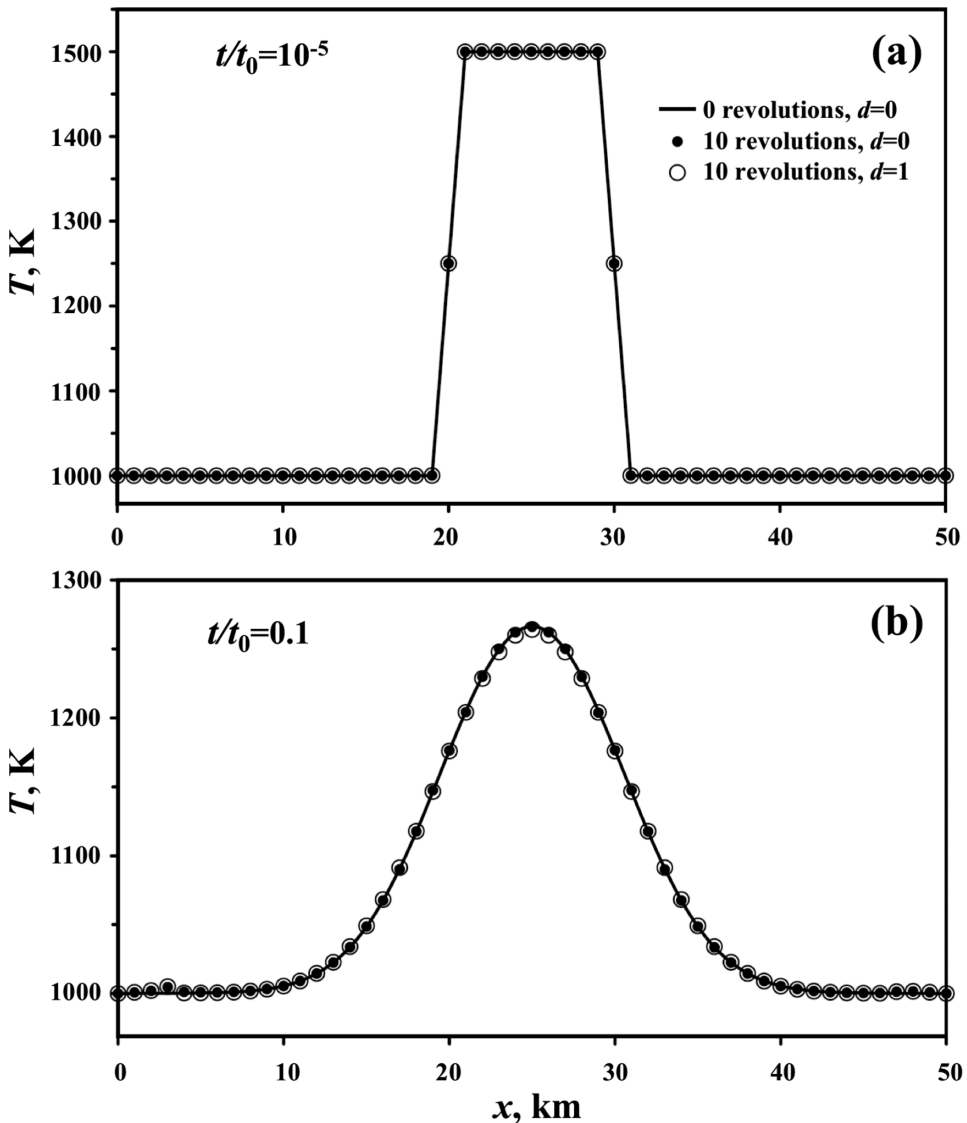


Fig. 20.7. The results of testing of the numerical solution for the solid body rotation of a square temperature wave. The figure shows the horizontal profiles across the wave at different times  $t$  after a given number of revolutions. (a) and (b) Results of numerical experiments at different characteristic thermal diffusion time scales  $t_0 = \rho C_P L^2 / k$ , where  $L = 10$  km is the initial length of the temperature wave.  $d$  is a numerical subgrid diffusion parameter (see Eq. 10.16 in Chapter 10). Numerical results are calculated at a resolution of  $51 \times 51$  nodes and  $250 \times 250$  markers with the code **Solid\_Body\_Rotation\_T.m**. Model parameters: size  $50 \times 50$  km $^2$ ,  $C_P = 1000$  J/(kg K),  $\rho = 3000$  kg/m $^3$ ,  $k = 2 \times 10^{-6}$  and  $0.02$  W/(m K) for (a) and (b), respectively,  $T_{\text{medium}} = 1000$  K,  $T_{\text{wave}} = 1500$  K. The small temperature perturbation at the left boundary in (b) is a boundary effect (i.e. a trace of the rotating wave interacting with the model thermal boundary condition; run program **Solid\_Body\_Rotation\_T.m** in order to see this trace in 2D).

program example **Variable\_viscosity\_Couette\_T.m**). Other parameters can again be computed with  $B$  from Eqs. (20.10)–(20.21). Figure 20.6 shows that numerical and analytical results coincide well, implying that the numerical solution holds for thermomechanical effects of shear heating in the case of strongly variable temperature-dependent viscosity.

## 20.7 Test 6: advection of sharp temperature fronts

Verification of the ability to advect sharp temperature fronts is fundamental in numerical tests of various advection algorithms. The geodynamic relevance of this test is obvious when modelling rapidly moving subducting and detached slabs is envisaged. Numerical solutions for this type of benchmark (see e.g. Chapter 8) are typically calculated in 2D for the solid body rotation of a two-dimensional temperature wave of an arbitrary shape. One can, for example, perform such a test for a square wave with width  $L$  and thermal amplitude  $\Delta T_0 = 500$  K. The results of the test obtained with our finite difference and marker-in-cell techniques are shown in Fig. 20.7 for a regularly spaced grid of moderate resolution ( $51 \times 51$  nodes,  $250 \times 250$  markers). If heat conduction is insignificant (Fig. 20.7a), the adopted marker-in-cell advection scheme is obviously not numerically diffusive, even for many revolutions, as far as the initial positions of markers (with the corresponding values of initially prescribed temperature field which is negligibly affected by the heat diffusion) are reproduced well with the classical fourth-order Runge–Kutta (Chapter 8) advection scheme (see code **Solid\_Body\_Rotation\_T.m**). In the case of significant heat conduction (Fig. 20.7b), the final temperature distribution does not depend noticeably on the number of revolutions. This point suggests good conservation properties of the adopted numerical scheme when advecting diffusing temperature fronts. Introducing numerical subgrid diffusion (Chapter 10) only negligibly affects the temperature when heat conduction is significant (Fig. 20.7b). Obviously, this numerical diffusion, which gives a small addition to the physical diffusion, exerts little influence in the case of negligible heat conduction (Fig. 20.7a). Generally, the tested method of solving the temperature equation using markers works very well in the two distinct regimes of advection for both non-diffusive (Fig. 20.7a) and diffusive (Fig. 20.7b) sharp temperature fronts.

## 20.8 Test 7: channel flow with variable thermal conductivity

This analytical benchmark can be conducted to verify the accuracy of a thermomechanical code in the case of strong variations in temperature-dependent thermal conductivity, which are relevant to many geodynamic situations that involve large variations in temperature (mantle convection, lithospheric processes, etc.). For this purpose, we can again use vertical Newtonian channel flow (as in test 4 but without temperature gradients along the channel) with a velocity distribution defined by Eq. (20.8) and shear heating, which provides a strong heat source term in the temperature equation (Chapter 9). The thermal conductivity is taken

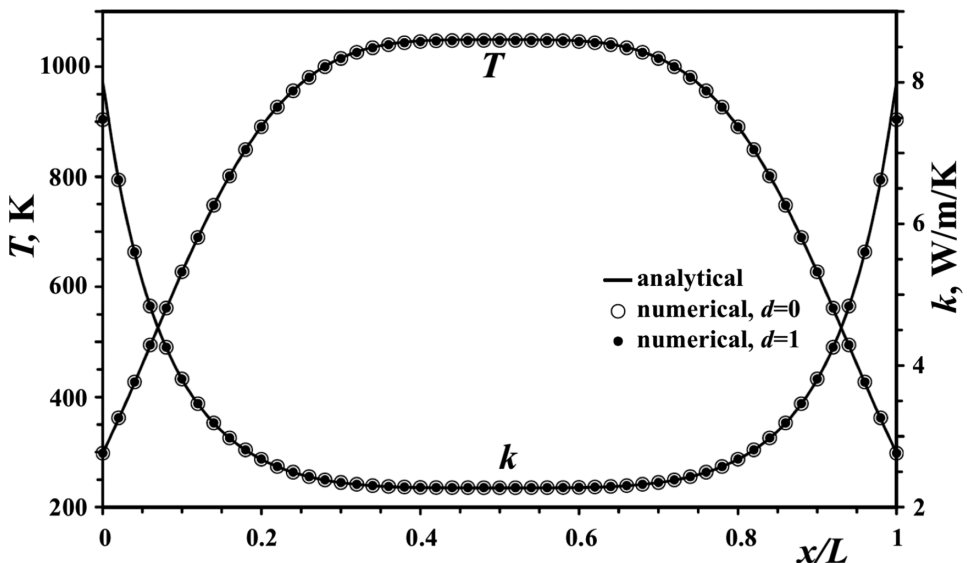


Fig. 20.8. Comparison of the analytical (Eq. 20.23) and numerical solutions for the steady temperature and thermal conductivity profiles across a channel with constant viscosity and strong shear heating. Numerical results are calculated at a resolution of  $51 \times 11$  nodes and  $250 \times 50$  markers with the code **Variable\_conductivity\_channel.m**. Model parameters:  $L = 30$  km,  $H = 11.25$  km,  $\eta = 10^{19}$  Pa s,  $P_{\text{beg}} = 3 \times 10^7$  Pa,  $P_{\text{end}} = 0$ ,  $T_0 = 298$  K,  $k_0 = 8$  W/(m K),  $b = 1$ .

to be decreasing with temperature, which is very characteristic (e.g. Hofmeister, 1999) for *lattice conductivity* defined by *phonons* in a crystal lattice

$$k = \frac{k_0}{1 + b(T - T_0)/T_0}, \quad (20.22)$$

where  $T_0$  is a constant temperature applied at the walls of the channel;  $k_0$  is the thermal conductivity at  $T_0$ ;  $b$  is a dimensionless coefficient.

The steady temperature profiles across the channel  $T(x)$  are then defined as (Gerya and Yuen, 2003a)

$$\begin{aligned} T(x) &= T_0 \frac{C(x) + b - 1}{b}, \\ C(x) &= \exp \left\{ \frac{L^4 b}{192 k_0 T_0 \eta} \left( \frac{\partial P}{\partial y} \right)^2 \left[ 1 - \left( 2 \frac{x}{L} - 1 \right)^4 \right] \right\}, \end{aligned} \quad (20.23)$$

where  $L$  is the channel width,  $\eta$  is a constant viscosity of the medium and  $\partial P/\partial y$  is the pressure gradient along the channel (Eq. 20.7).

Figure 20.8 compares the analytical solution for both temperature and thermal conductivity profiles with the numerical solutions obtained with the 2D thermomechanical code

**Variable\_conductivity\_channel.m.** This figure demonstrates the high accuracy of the numerical solution, suggesting that the adopted conservative FD scheme correctly computes heat transport in the case of strong variations in thermal conductivity (factor of 4 variation across the channel for the given case, Fig. 20.8).

## 20.9 Test 8: thermal convection with constant and variable viscosity

This benchmark can be conducted to test the ability of the code to model mantle convection. Blankenbach et al. (1989) tested several 2D mantle convection models with a broad variety of numerical techniques and reported steady-state values for a number of model parameters to which the numerical solution should converge with increasing grid resolution. Table 20.1 represents the physical parameters for five steady-state convection models with both constant (models 1a, 1b, 1c) and variable (models 2a, 2b) temperature- and depth-dependent viscosity. Convection is studied in a rectangular box of height  $H$  and width  $L$  ( $H = L = 1000$  km for all models with the exception of model 2b). The boundary conditions are free slip along all boundaries, a specified temperature on the top ( $T_{top}$ ) and at the bottom ( $T_{bottom}$ ) and thermal insulation ( $\partial T / \partial x = 0$ ) along the left and right walls. The difference between  $T_{top}$  and  $T_{bottom}$  in all experiments is 1000 K. The following formulation for temperature- and depth-dependent viscosity of the mantle is used:

$$\eta = \eta_0 \exp\left(-b \frac{T - T_{top}}{T_{bottom} - T_{top}} + c \frac{y}{H}\right), \quad (20.24)$$

where  $\eta_0$  is viscosity at the top of the model (i.e. at  $T = T_{top}$  and  $y = 0$ );  $b$  and  $c$  are coefficients establishing the dependences of viscosity with temperature and depth, respectively ( $b = 0$  and  $c = 0$  in constant viscosity tests 1a, 1b and 1c). Density in all models depends linearly on temperature

$$\rho = \rho_0 [1 - \alpha(T - T_{top})],$$

where  $\rho_0 = 4000$  kg/m<sup>3</sup> is the standard density and  $\alpha = 2.5 \times 10^{-5}$  1/K is the thermal expansion coefficient.

Despite this relatively simple setup, obtaining an accurate steady-state solution for mantle convection models is quite challenging. This is mainly due to (i) many (typically several thousand) time steps required to obtain a steady-state solution and (ii) a strong localization of thermal upwellings and downwellings along the walls (e.g. Fig. 20.9c) in models with low mantle viscosity (or more precisely with high *Rayleigh number*  $Ra = \rho_0 \alpha (T_{bottom} - T_{top}) g_y H^3 C_P / (\eta k)$ , where  $g_y$  is the vertical component of the gravitational acceleration,  $C_P$  is the isobaric heat capacity and  $k$  is the thermal conductivity). The problem of localization can be overcome either by using a high resolution for the entire model or (more efficiently) by using an irregularly spaced grid, which is denser at the model walls (Fig. 20.9a). The steady-state thermal structures computed for some of the

Table. 20.1 Parameters of mantle convection benchmarks (Blankenbach et al., 1989)

Test	1a	1b	1c	2a	2b
Gravitational acceleration, $g$ (m/s <sup>2</sup> )	10	10	10	10	10
Model height, $H$ (km)	1000	1000	1000	1000	1000
Model width, $L$ (km)	1000	1000	1000	1000	2500
Temperature at the top, $T_{top}$ (K)	273	273	273	273	273
Temperature in the bottom, $T_{bottom}$ (K)	1273	1273	1273	1273	1273
Thermal conductivity, $k$ (W/(m K))	5	5	5	5	5
Heat capacity, $C_P$ (J/kg)	1250	1250	1250	1250	1250
Standard density, $\rho_0$ (kg/m <sup>3</sup> )	4000	4000	4000	4000	4000
Thermal expansion, $\alpha$ (1/K)	$2.5 \times 10^{-5}$				
Flow law parameters: $\eta_0$ (Pa s)	$10^{23}$	$10^{22}$	$10^{21}$	$10^{23}$	$10^{23}$
$b$	0	0	0	ln(1000)	ln(16384)
$c$	0	0	0	0	ln(64)
Nusselt number, $Nu = \frac{H}{T_{bottom}L} \int_{x=0}^L \left( \frac{\partial T}{\partial y} \right)_{top} dx$	4.8844	10.534	21.972	10.066	6.9229
Non-dimensional root mean square (rms) velocity,	42.865	193.21	833.99	480.43	171.76
$v_{rms} = \frac{H\rho_0 C_P}{k} \sqrt{\frac{1}{HL} \int_{x=0}^L \int_{y=0}^H (v_x^2 + v_y^2) dy dx}$					
Non-dimensional temperature gradients in the model corners,					
$q_{corner} = \frac{H}{T_{bottom} - T_{top}} \left( \frac{\partial T}{\partial y} \right)_{corner}$					
$q_1$ (top-left corner, above upwelling)	8.0593	19.079	45.964	17.531	18.484
$q_2$ (top-right corner, above downwelling)	0.5888	0.7228	0.8772	1.0085	0.1774
$q_3$ (bottom-right corner, below downwelling)	8.0593	19.079	45.964	26.809	14.168
$q_4$ (bottom-left corner, below upwelling)	0.5888	0.7228	0.8772	0.4974	0.6177
Local minimum along the central vertical temperature profile: $T_c = \frac{T - T_{top}}{T_{bottom} - T_{top}}$	0.4222	0.4284	0.4322	0.7405	0.3970
$Z_c = \frac{H - y}{H}$	0.2249	0.1118	0.0577	0.0623	0.1906
Local maximum along the central vertical temperature profile: $T_c = \frac{T - T_{top}}{T_{bottom} - T_{top}}$	0.5778	0.5716	0.5678	0.8323	0.5758
$Z_c = \frac{H - y}{H}$	0.7751	0.8882	0.9423	0.8243	0.7837

models of Table 20.1 are shown in Fig. 20.9b,c,d. Figure 20.10 presents the results of the mantle convection benchmark for these models obtained with the program **Variable\_viscosity\_convection\_irregular\_grid.m** associated with this chapter. As can be seen at the same model resolution of  $51 \times 51$  nodes and 40 000 markers, models with an irregularly spaced grid show results that are much closer to the benchmark values.

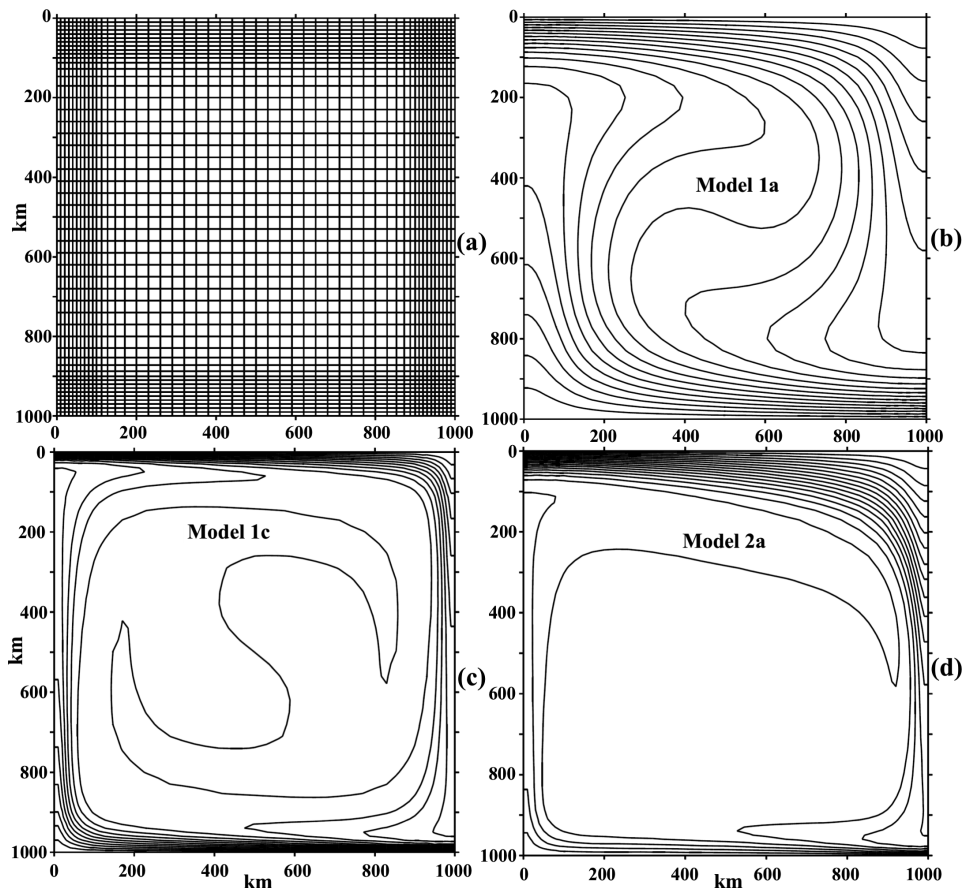


Fig. 20.9. Irregularly (10–30 km) spaced grid (a) and steady-state temperature structures (b)–(d) for the three mantle convection benchmarks from Table 20.1. Numerical results are computed at a resolution of  $51 \times 51$  nodes and  $200 \times 200$  randomly distributed markers with the code **Variable\_viscosity\_convection\_irregular\_grid.m**. Solid lines in (b)–(d) represent isotherms between  $T_{top}$  and  $T_{bottom}$  with an interval of 50 K.

Therefore the use of adaptive irregularly spaced grids (based on ‘Swiss cross’ AMR, Chapter 17), can in many cases significantly increase the accuracy of the numerical solution without a notable increase in computational cost.

## 20.10 Test 9: stress buildup in a visco-elastic Maxwell body

This test can be performed to verify the 2D numerical solutions for the case of a deforming visco-elastic Maxwell body (Exercise 12.1). In the case of uniform pure shear, deformation of an initially unstressed, incompressible visco-elastic medium with a constant strain rate  $\dot{\varepsilon}_{xx}$ , elastic deviatoric stress  $\sigma'_{xx}$ , grows with time  $t$  according to the equation

$$\sigma'_{xx} = 2\dot{\varepsilon}_{xx}\eta[1 - \exp(-t\mu/\eta)], \quad (20.25)$$

where  $t$  is the time from the beginning of deformation and  $\eta$  and  $\mu$  are the constant viscosity and shear modulus of the medium, respectively. Based on Eq. (20.25), one can perform a numerical test of stress buildup shown in Fig. 20.11. The numerical experiment is designed on a rectangular model (cf. panel in Fig. 20.11) by prescribing constant outward directed velocity  $v_x$  along the vertical boundaries and inward directed velocity  $v_y$  for the horizontal boundaries of the model computed as

$$v_x = \frac{1}{2}\dot{\varepsilon}L_x,$$

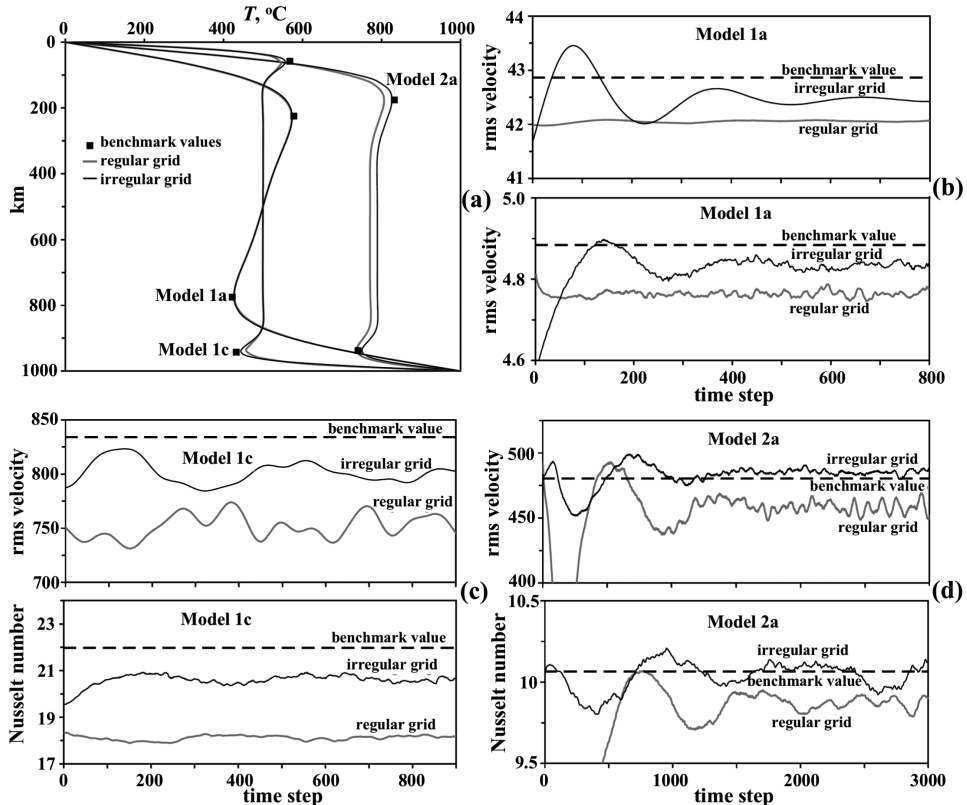


Fig. 20.10. Vertical steady-state temperature profiles in the centre of the model (a) and near-steady-state variations of root mean square (rms) velocity and Nusselt number (b)–(d) for the three mantle convection benchmarks from Table 20.1. Dashed lines in (b)–(d) show the benchmark values for respective parameters from Table 20.1. Solid lines show the numerical results calculated at a resolution of  $51 \times 51$  nodes and  $200 \times 200$  randomly distributed markers with the code `Variable_viscosity_convection_irregular_grid.m`.

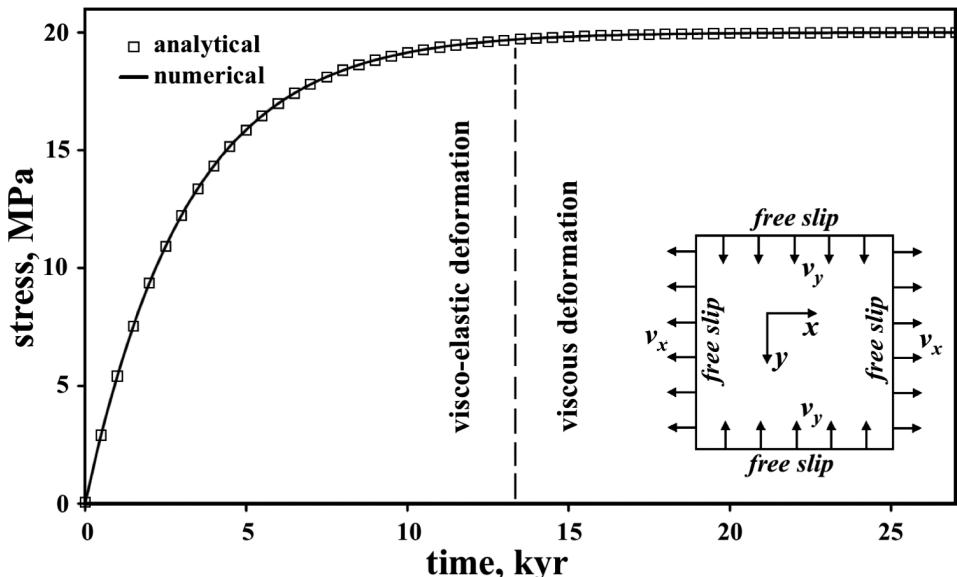


Fig. 20.11. Comparison of numerical (symbols) and analytical (solid line) solutions for the case of visco-elastic stress buildup due to pure shear ( $x$ - $y$  direction) with constant normal strain rate and in the absence of gravity. Numerical and analytical (Eq. 20.25) solutions are compared for  $\dot{\varepsilon}_{xx} = 10^{-14} \text{ s}^{-1}$ ,  $\eta = 10^{21} \text{ Pa s}$  and  $\mu = 10^{10} \text{ Pa}$ . The panel with numerical setup is shown in the right part of the diagram. Numerical results are calculated at a resolution of  $51 \times 51$  nodes and  $200 \times 200$  markers with the code **Stress\_buildup.m**.

$$v_y = \frac{1}{2}\dot{\varepsilon}L_y,$$

where  $\dot{\varepsilon}$  is prescribed deviatoric strain rate, and  $L_x$  and  $L_y$  are respectively horizontal and vertical dimensions of the model. At each time step, all deviatoric stress components are interpolated from markers (either regularly or randomly distributed) to nodes, and stress increments are then interpolated back to markers (Fig. 13.1 in Chapter 13) after numerically solving the momentum and continuity equations for the entire model domain. Figure 20.11 is computed with the code **Stress\_buildup.m** and demonstrates the high accuracy of the numerical solution, which overlaps with the analytical one, hence properly describing the transition from the dominant elastic regime to the prevailing viscous deformation.

### 20.11 Test 10: recovery of the original shape of an elastic slab

This benchmark can be performed to test the 2D visco-elastic numerical solutions in terms of proper advection and conservation of elastic stresses. Figure 20.12 shows the results of a numerical experiment for the recovery of the original shape of an elastic slab surrounded by a low density medium with much lower viscosity and much higher shear modulus than the slab.

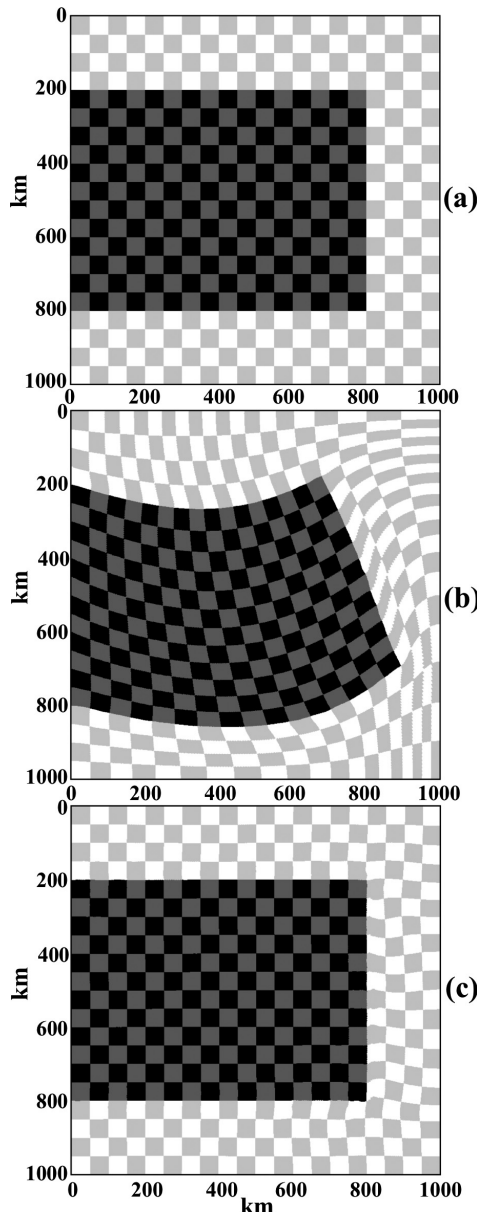


Fig. 20.12. Results of a numerical experiment for the recovery of the original shape of a visco-elastic slab (black, dark grey,  $\rho = 4000 \text{ kg/m}^3$ ,  $\eta = 10^{27} \text{ Pa s}$  and  $\mu = 10^{10} \text{ Pa}$ ) embedded in a weak visco-elastic medium (light grey, white,  $\rho = 1 \text{ kg/m}^3$ ,  $\eta = 10^{21} \text{ Pa s}$  and  $\mu = 10^{20} \text{ Pa}$ ). (a) Initial configuration. (b) Configuration after 20 kyr of deformation under constant vertical gravity field ( $g_x = 0$ ,  $g_y = 10 \text{ m/s}^2$ ). (c) Configuration achieved within 9980 kyr of spontaneous deformation after switching off gravity (i.e. after the condition  $g_x = g_y = 0$  is applied at 20 kyr). Boundary conditions: no slip at the left boundary and free slip at all other boundaries. Numerical results are calculated at a resolution of  $51 \times 51$  nodes and  $200 \times 200$  markers with the code **Slab\_deformation.m** associated with this chapter. Note the irreversible viscous deformation of the weak surrounding medium, which is visible in its perturbed checkerboard structure close to slab corners in (c).

The initially unstressed slab is attached to the left wall of the box and is spontaneously deformed within 20 kyr under a purely vertical gravity field ( $g_y = 10 \text{ m/s}^2$ ,  $g_x = 0$ ). The slab deformation is purely elastic due to the large Maxwell time (3 170 000 kyr) of slab material compared to the total deformation time (20 000 kyr). In contrast, the low viscosity medium is subjected to irreversible, purely viscous deformation since its Maxwell time ( $3.17 \times 10^{-10}$  kyr) is negligible compared to the deformation time. The degree of elastic deformation in the slab is large (Fig. 20.12b) and the stresses stored on markers are, therefore, subjected to significant advection and rotation under both simple shear and pure shear deformation. After gravity is ‘switched off’ (i.e. after the condition  $g_x = g_y = 0$  is set), the slab starts to unbend and finally fully recovers its original shape (Fig. 20.12c). In contrast, the low density medium does not recover its original configuration since the viscous deformation is irreversible (see perturbations of the checkerboard pattern in the weak medium around the slab corners).

For the model shown in Fig. 20.12, the deformation rate is independent of time step and is fully determined by the viscosity of the low density medium, which acts as a stronger material (note upbending of the lower right edge of the slab in response to the flow of the low density medium around the slab). This relationship is caused by the lower shear modulus of the slab ( $10 \times 10^{10} \text{ Pa}$ ) compared to that of the low density medium ( $10 \times 10^{20} \text{ Pa}$ ). In contrast, in Figure 12.2 from Chapter 12, another situation is shown (Gerya and Yuen, 2007) where shear moduli of both materials are the same and the low density medium acts as a weak material. The character of slab deformation changes correspondingly (dominant simple shear deformation and no significant upbending). In this case, however, the deformation rate is time step dependent, which does not preclude, indeed, testing the slab shape recovery (Fig. 12.2).

## 20.12 Test 11: numerical sandbox benchmark

Let us also consider the comparison of numerical results with physical (analogue) sandbox experiments. Numerical modelling of sandbox experiments poses significant computational challenges because the numerical code must be able (1) to calculate large strains along spontaneously forming narrow shear zones, (2) to represent complex boundary conditions, including frictional boundaries and free surfaces, and (3) to include a complex rheology involving both viscous and frictional/plastic materials. These challenges reflect directly the state of the art requirements for numerical modelling of large-scale tectonic processes. Several numerical sandbox benchmarks were described by Buiter et al. (2006, 2016), in which the results of analogue and numerical experiments for both shortening (Fig. 20.13) and extension settings were compared. One of the shortening experiments (Buiter et al., 2006) was conducted with the use of a mobile wall moving leftward at a velocity of 2.5 cm/hour (Fig. 20.13a). The original cross-section is composed of sand (density  $\rho = 1560 \text{ kg/m}^3$ , cohesion  $C = 10 \text{ Pa}$ , an initial internal friction angle of  $\varphi_{\text{initial}} = 36^\circ$  which changes linearly to the stable value of  $\varphi_{\text{stable}} = 31^\circ$  with strain increasing

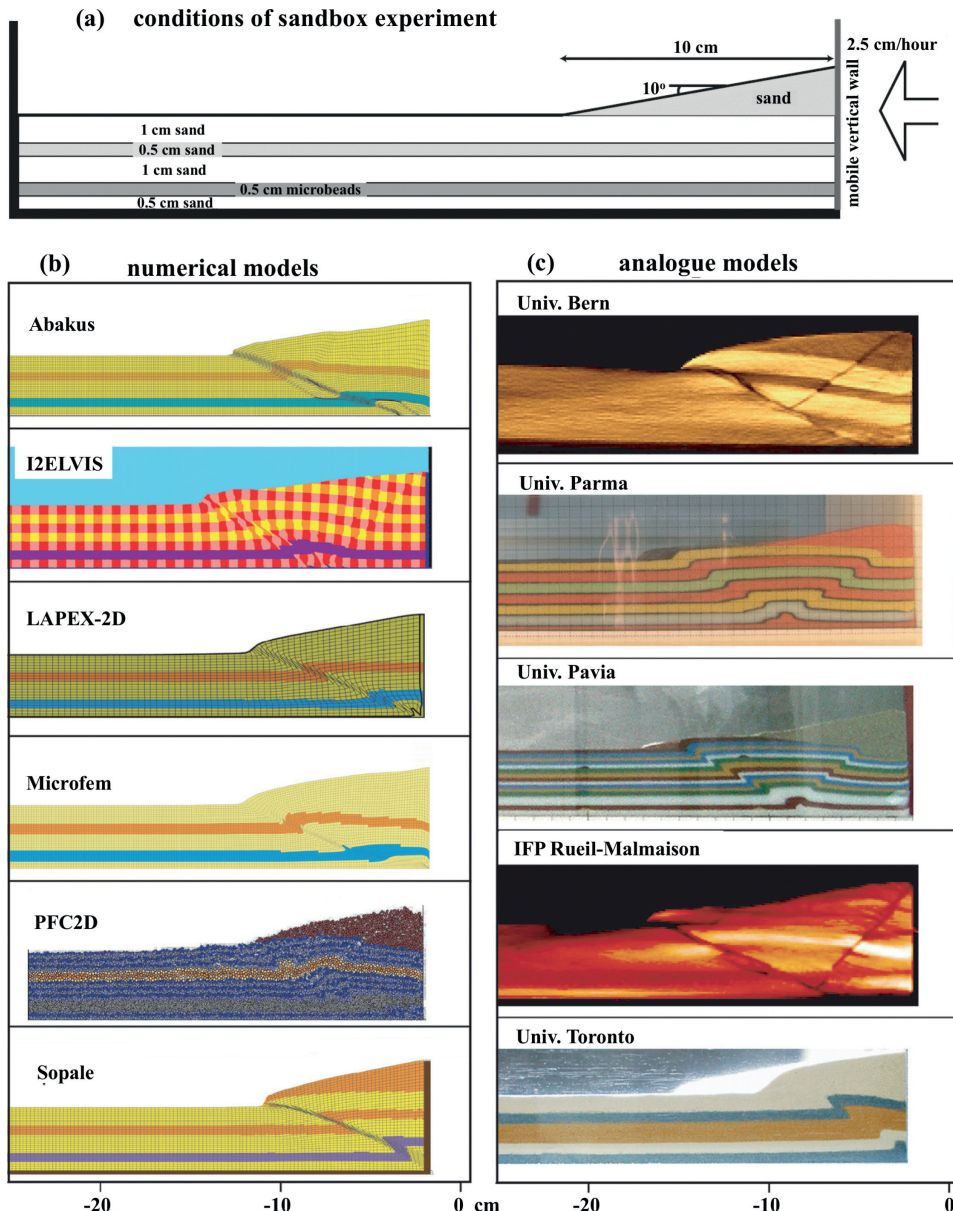


Fig. 20.13. Setup of a shortening experiment (a) and comparison of numerical (b) and analogue (c) models (at ~2 cm of shortening) performed by Buiter et al. (2006). (a) Horizontal layers of ‘sand’ (which have the same properties and differ in colour only) with an embedded layer of weaker ‘microbeads’ are shortened through a mobile wall on the right hand side which is pushed leftwards. (b),(c) Names of numerical codes (b) and analogue laboratories (c) are given in the respective model boxes.

from 0 to 1) and includes a 0.5 cm thick weak layer of microbeads ( $\rho = 1480 \text{ kg/m}^3$ ,  $C = 10 \text{ Pa}$ ,  $\varphi_{initial} = 22^\circ$ ,  $\varphi_{stable} = 20^\circ$ ). In the right part, the model includes a 10 cm wide surface wedge composed of sand. Boundary friction on all sandbox walls is lowered ( $C = 0$ ,  $\varphi_{initial} = 19^\circ$ ,  $\varphi_{stable} = 19^\circ$ ). Boundary conditions corresponding to the mobile wall can be implemented in a number of ways. One option is to include a rigid (highly viscous) mobile wall and prescribe constant velocity conditions ( $v_x = -2.5 \text{ cm/hour}$ ,  $v_y = 0$ ) on Eulerian nodes located inside this wall (Fig. 20.14a). This can be done in combination with a weak layer included in the model, which simulates air and shifts behind the wall as it moves. In order to ensure that the wall does not leave nodes with prescribed velocity, it can be thickened from behind, by accreting displaced air markers (Fig. 20.14b). It should be pointed out that the implementation of the mobile wall condition may notably affect the results of numerical experiments: for example, a backthrust that forms in most of the analogue experiments is absent in many numerical models where a mobile wall condition is implemented by prescribing a shortening velocity directly on the right model boundary (cf. Fig. 20.13b and 20.13c). The numerical and analogue models share many similarities (Buiter et al., 2006).

- (1) Shortening is accommodated by an in-sequence forward propagation of thrusts (Fig. 20.14c, also see Fig. 12.6 in Chapter 12).
- (2) The first-formed thrust roots at the base of the mobile wall (Fig. 20.14c).
- (3) By 2 cm of displacement, an active thrust has formed in all models (Figs. 20.13b,c, 20.14c).
- (4) The location where the first-formed forward thrust reaches the surface is influenced by the surface wedge in almost all of the experiments (Figs. 20.13b,c, 20.14c).

It should be pointed out, however, that details of shear zone patterns formed in individual analogue and numerical models are strongly variable. Such variations are an intrinsic feature of plastic deformation, and reproducing the exact pattern of shear zones should not be considered as the benchmarking goal. More importantly, with this benchmark a numerical code should rather demonstrate its ability to hold for large deformation, for strong strain localization along spontaneously forming narrow (1–2 grid cell wide) shear zones and for reproducing the general structural pattern of both forward and backward faults formed in analogue experiments. Figure 20.14 shows the results of the numerical sandbox experiments obtained with the code **Sandbox\_shortening\_ratio.m**. The differences between the numerical and analogue models are on the same order as the differences between analogue models from different laboratories (cf. Figs. 20.13b,c, 20.14b,c). The implemented numerical approach of plasticity treatment (Chapters 12 and 13) allows for spontaneous onset of narrow shear zones, which forms a sequence of forward and backward faults like in analogue experiments.

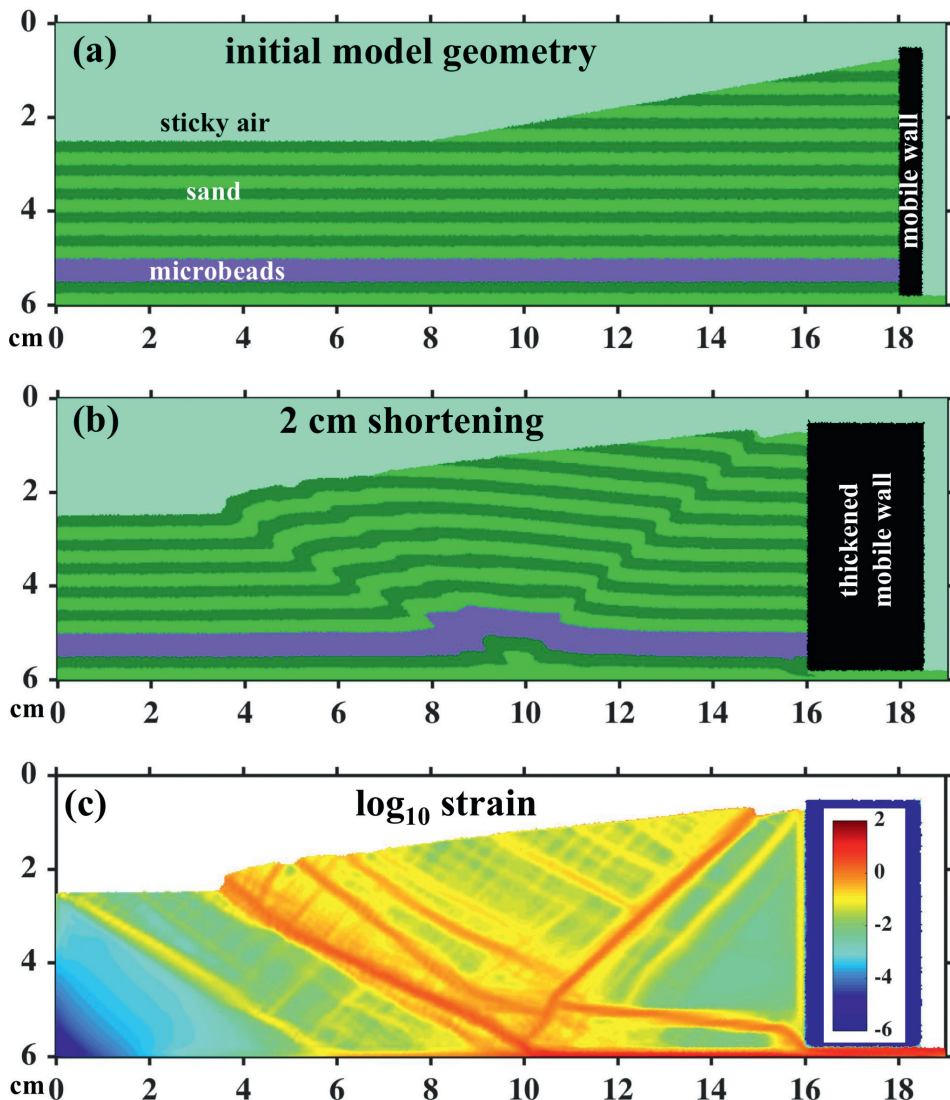


Fig. 20.14. Initial setup (a) and results (b),(c) of the numerical experiment for the shortening benchmark (Fig. 20.13a). The numerical model employs a visco-elasto-plastic rheology with the following material properties: sand (light green, green),  $\rho = 1560 \text{ kg/m}^3$ ,  $C = 10 \text{ Pa}$ ,  $\varphi_{\text{initial}} = 36^\circ$ ,  $\varphi_{\text{stable}} = 31^\circ$ ,  $\eta = 10^9 \text{ Pa s}$ ,  $\eta = 10^6 \text{ Pa}$ ; microbeads (blue),  $\rho = 1480 \text{ kg/m}^3$ ,  $C = 10 \text{ Pa}$ ,  $\varphi_{\text{initial}} = 22^\circ$ ,  $\varphi_{\text{stable}} = 20^\circ$ ,  $\eta = 10^9 \text{ Pa s}$ ,  $\mu = 10^6 \text{ Pa}$ ; weak layer ('sticky air', very light green),  $\rho = 1 \text{ kg/m}^3$ ,  $\eta = 10^2 \text{ Pa s}$ ,  $\mu = 10^6 \text{ Pa}$ ; mobile wall (black),  $\rho = 1520 \text{ kg/m}^3$ ,  $\eta = 10^{12} \text{ Pa s}$ ,  $\mu = 10^{16} \text{ Pa}$ . Boundary conditions: no slip at the left and bottom boundaries and free slip on all other boundaries. Boundary friction is implemented by prescribing  $\varphi_{\text{initial}} = \varphi_{\text{stable}} = 19^\circ$  for sand and microbeads located within 2 mm of the lower and left boundaries and of the mobile wall. The shortening condition ( $v_x = -2.5 \text{ cm/hour}$ ,  $v_y = 0$ ) is prescribed on the Eulerian nodes located inside the mobile wall. Note that the mobile wall is separated from the bottom by a 2 mm thick layer of sand and is thickening from the right by converting markers of the displaced 'sticky air'. Numerical results are calculated at a resolution of  $191 \times 61$  nodes with 182 400 randomly distributed markers by using the code **Sandbox\_shortening\_ratio.m**.

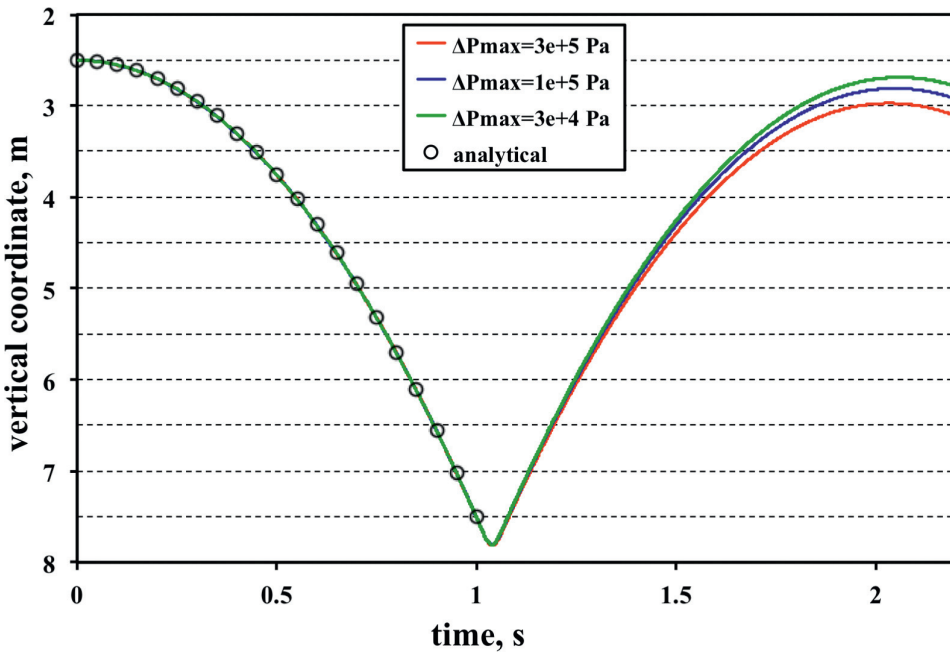


Fig. 20.15. Results of a numerical experiment for an elastic ball bouncing in a constant vertical gravity field ( $g_x = 0$ ,  $g_y = 10 \text{ m/s}^2$ , Fig. 14.3a). Material properties: ball,  $\rho = 3000 \text{ kg/m}^3$ ,  $\eta = 10^{22} \text{ Pa s}$ ,  $\rho = 10^8 \text{ Pa}$ ,  $\beta = 10^{-8} \text{ 1/Pa}$ , sticky air,  $\rho = 1 \text{ kg/m}^3$ ,  $\eta = 10^{-3} \text{ Pa s}$ ,  $\mu = 10^8 \text{ Pa}$ ,  $\beta = 10^{-8} \text{ 1/Pa}$ . Different curves show changes of vertical position of the ball centre with time for different time stepping conditions limited by the maximal allowed changes in deviatoric stresses and pressure per time step ( $\Delta P_{\max}$ ). Numerical results are calculated at a resolution of  $51 \times 51$  nodes and  $200 \times 200$  markers with the code **Bouncing\_Ball.m** associated with this chapter.

## 20.13 Test 12: bouncing ball benchmark

This simple elegant benchmark (Zhigadla, 2015) can be performed to test the 2D viscoelastic compressible numerical solutions with inertia (Chapter 14) in terms of proper conversion of kinetic energy into stresses and back. The numerical setup consists of a circular elastic object ('ball') surrounded by the sticky air (Fig. 14.3a, Exercise 14.2). The ball falls freely downward in the vertical gravity field until it collides with the lower model boundary and starts to deform elastically. Elastic deformation consumes kinetic energy of the ball by converting it into deviatoric stresses and pressure, thereby changing the velocity of the ball. As a result, the ball is reflected by the boundary and accelerates in the upward direction until all accumulated deviatoric stresses and pressure are released. Then the ball flies upward, being decelerated by the gravity field until its velocity goes to zero and it starts to fall back. If the deformation of the ball is purely elastic (i.e. fully reversible) and the numerical algorithm is robust, then the ball should keep bouncing without losing its potential energy and should always

recover its original maximal altitude (or at least this altitude should decrease very slowly). Figure 20.15 shows the results of a numerical experiment for the recovery of the original altitude of the ball after the first bounce obtained with the code **Bouncing\_Ball.m**. It can be seen that the quality of recovery mainly depends on the time stepping condition limited by the maximal allowed changes in deviatoric stresses and pressure per time step (Chapter 14). The smaller the allowed stress and pressure changes are the shorter the time step during the collision of the ball with the lower boundary and the more accurate the conversion of the kinetic energy into stresses and back. The results of this benchmark show that the SFD-MIC numerical algorithm discussed in Chapter 14 is robust and can be successfully used for accurate modelling of impact processes (Zhigadla, 2015).

## 20.14 Possible further benchmarks

Obviously, the potential number of benchmarks for testing numerical codes is infinite and not all of them are described in the present chapter. A few additional references for further numerical benchmarking problems are listed below:

- 2D analytical solutions for mantle thermal convection (Hager and O'Connell, 1981; Revenaugh and Parsons, 1987);
- 2D thermochemical convection (van Keken et al., 1997);
- 2D viscoplastic thermal convection (Tosi et al., 2015);
- 2D buoyancy-driven flows for strongly varying viscosity in the horizontal and vertical directions (Moresi et al., 1996; Zhong, 1996);
- 2D flow around deformable elliptic inclusions (Schmid and Podladchikov, 2003; Deubelbeiss and Kaus, 2008);
- 2D visco-elastic Rayleigh–Taylor instability (Kaus and Becker, 2007);
- 2D thermomechanical corner flows in subduction zones (van Keken et al., 2008);
- 2D spontaneous subduction with a free surface (Schmeling et al., 2008);
- 2D solitary waves in magma dynamics (Simpson and Spiegelman, 2011);
- 2D and 3D Stokes flow with variable viscosity (Popov et al., 2014b);
- 3D mantle convection in Cartesian geometry (Busse et al., 1994);
- 3D mantle convection in spherical geometry (Zhong et al., 2008);
- 3D infinitesimal and finite amplitude folding instability (Kaus and Schmalholz, 2006);
- 3D viscous incompressible Stokes flow in a spherical shell (Thieulot, 2017).

## 20.15 Method of manufactured solutions

One flexible and powerful approach to developing analytical solutions for geodynamic benchmarks is the *method of manufactured solutions* (MMS) (e.g. Roache, 1997, 1998; Dohrmann and Bochev, 2004; Galvan and Miller, 2013; May et al., 2013; Thieulot, 2014).

The MMS technique allows for the construction of arbitrarily complex solutions to any linear, or non-linear PDE. For Stokes flow problems, the MMS consists of prescribing some analytical functions (typically satisfying the incompressibility condition) for velocity components, viscosity and pressure to express their dependence on spatial coordinates (e.g. Dohrmann and Bochev, 2004). Based on these functions, boundary conditions and right parts of the conservation equations (e.g., buoyancy terms,  $\rho g$ ) are computed analytically, and the solutions are used for prescribing the internal model geometry. Accuracy of the numerical code is tested by comparing coupled numerical solutions of Stokes and continuity equations for the manufactured model with the originally prescribed analytical functions for velocity components and pressure. At present, the MMS is not commonly used in geodynamic modelling (e.g. Galvan and Miller, 2013; May et al., 2013; Thieulot, 2014), in stark contrast to the applied mathematics and engineering communities (e.g. Roache, 1997, 1998; Dohrmann and Bochev, 2004). Exploiting the MMS in computational geodynamics will help to establish a higher level of robustness and reliability in both the numerical methods used, and in the verification of their implementation (May et al., 2013).

## Programming exercises

### Exercise 20.1.

Program an external MATLAB function for the 2D pressure-velocity Stokes+continuity variable viscosity solver for a regular staggered grid with external velocity nodes (Figs. 7.16, 18.8) based on the ghost node approach (Eqs. 18.39–18.42) and respective global indexing of unknowns as discussed in Chapter 7 (Fig. 7.16). Implement this solver in your viscous thermomechanical code (programming exercise 11.1 of Chapter 11). With this new viscous code, perform the falling block benchmark and compare the results with Figs. 20.2 and 20.3. The model setup corresponds to Fig. 20.2. An example is provided in **Variable\_viscosity\_block.m**.

### Exercise 20.2.

Implement the ghost node based solver from the previous example into your visco-elastic thermomechanical code (Exercise 13.1). With this new code, perform the visco-elastic slab bending benchmark and compare the results with Fig. 20.12. The model setup corresponds to Fig. 20.12. An example is provided in **Slab\_deformation.m**.

### Exercise 20.3.

Modify Exercise 7.2 to build a 2D manufactured solution benchmark for isoviscous ( $\eta = 10^{19}$  Pa s) incompressible Stokes flow with the following velocity and pressure fields defined analytically (cf. Exercise 1.2)

$$v_x = -v_{x0} \sin\left(2\pi \frac{x}{W}\right) \cos\left(\pi \frac{y}{H}\right),$$

$$v_y = v_{y0} \cos\left(2\pi \frac{x}{W}\right) \sin\left(\pi \frac{y}{H}\right),$$

$$P = P_0 + y \frac{\partial P_0}{\partial y} + \Delta P \cos\left(2\pi \frac{x}{W}\right) \sin\left(\pi \frac{y}{H}\right),$$

where  $x$  and  $y$  are respectively horizontal and vertical coordinates inside the box in metres;  $W = 1\,000\,000$  m and  $H = 1\,500\,000$  m are the width and height of the model, respectively;  $v_{x0} = 1 \times 10^{-9}$  m/s and  $v_{y0} = 3 \times 10^{-9}$  m/s are scaling values for respectively horizontal and vertical velocity components;  $P_0 = 10^5$  Pa,  $\partial P_0 / \partial y = 33\,000$  Pa/m and  $\Delta P = 10^6$  Pa are parameters of the pressure field. Derive analytical expressions for the right parts (i.e.,  $\rho g_x$  and  $\rho g_y$  terms) of the following simplified  $x$  Stokes and  $y$  Stokes equations valid for incompressible constant viscosity flows (Chapter 5)

$$\eta \left( \frac{\partial^2 v_x}{\partial x^2} + \frac{\partial^2 v_x}{\partial y^2} \right) - \frac{\partial P}{\partial x} = -\rho g_x,$$

$$\eta \left( \frac{\partial^2 v_y}{\partial x^2} + \frac{\partial^2 v_y}{\partial y^2} \right) - \frac{\partial P}{\partial y} = -\rho g_y.$$

Use these expressions to compute the right parts of the discretized  $x$  Stokes and  $y$  Stokes equations using  $x$  and  $y$  coordinates of respective staggered velocity nodes. Compare the analytical and numerical solutions for velocity and pressure and visualize their differences. Check the influence of the model resolution on the numerical accuracy. An example is provided in **Manufactured.m**.